nature communications

Article

https://doi.org/10.1038/s41467-025-60172-y

# Stable narrowband blue OLEDs by modulating frontier molecular orbital levels

Received: 23 December 2024

Accepted: 16 May 2025

Published online: 28 May 2025

Check for updates

Xiao-Chun Fan[1,2,7], Xun Tang[2,7] ✉, Tong-Yuan Zhang[1], Shintaro Kohata[2], Jia Yu[1,3], Xian-Kai Chen[1], Kai Wang[1,4] ✉, Takuji Hatakeyama[5], Chihaya Adachi[2,6] ✉ & Xiao-Hong Zhang[1,3] ✉

Energy level alignment of frontier molecular orbital (FMO) is essential for controlling charge carrier and exciton dynamics in organic light-emitting diodes (OLEDs). However, multiple resonance (MR) emitters with exceptional narrowband luminescence typically suffer from inadequate FMO levels. Herein, a conventional blue MR prototype with a shallow highest occupied molecular orbital (HOMO) level of −5.32 eV is initially employed to reveal the charge carrier and exciton dynamics. Severe hole trapping by its shallow HOMO significantly hinders its transport. More importantly, trapped carriers induce direct exciton formation and recombination at MR emitters in a hyperfluorescent system, leading to triplet accumulation in MR emitters. To resolve these issues, a proof-of-concept wavefunction perturbation strategy is proposed by incorporating cyano motifs at peripheral sites of MR backbone to adjust the energy levels. This approach significantly shifts HOMOs of 0.36 and 0.51 eV without compromising colour purity. The derivative substituting *meta*-boron position (*m*CNDB) exhibits a pure-blue emission peaking at 459 nm with a narrow bandwidth of 13 nm. The detrimental carrier trapping effect is eliminated, enhancing external quantum efficiency to exceeding 23%, maintaining around 20% at 1000 cd $m^{-2}$, and improving the device stability.

Comprehending and manipulating the energy level alignments of functional molecules is essential for determining the behaviours of charge carriers and excitons in optoelectronic devices. This is particularly crucial for blue organic light-emitting diodes (OLEDs). Simultaneously achieving high efficiency, stability, and colour purity has been the most challenging topic since the first two-layer OLED was reported by C. W. Tang and S. A. VanSlyke in 1987[1]. Regarding efficiency, the fundamental breakthrough of the charge-transfer (CT) state has allowed the creation of numerous efficient emitters, induced by metal-ligand CT and thermally activated delayed fluorescence (TADF) molecules[2–4]. By versatilely utilizing spin-forbidden triplets for radiation, a unity internal quantum efficiency, as well as a high external quantum efficiency (EQE), has been realized with adequate device architectures[5–8]. Furthermore, by leveraging the multiple resonance (MR) effect, an extremely narrow spectral width of less than 20 nm can be achieved by MR-TADF molecules by suppressing the intramolecular vibrations and relaxation in their excited states[9–12].

[1]Institute of Functional Nano & Soft Materials (FUNSOM), Joint International Research Laboratory of Carbon-Based Functional Materials and Devices, Soochow University, Suzhou, Jiangsu, China. [2]Center for Organic Photonics and Electronics Research (OPERA), Kyushu University, 744 Motooka, Nishi-ku, Fukuoka, Japan. [3]Jiangsu Key Laboratory of Advanced Negative Carbon Technologies, Soochow University, Suzhou, Jiangsu, China. [4]Jiangsu Key Laboratory for Carbon-Based Functional Materials & Devices, Soochow University, Suzhou, Jiangsu, China. [5]Department of Chemistry, Graduate School of Science, Kyoto University, Kitashirakawa Oiwake-cho, Sakyo-ku, Kyoto, Japan. [6]International Institute for Carbon-Neutral Energy Research (I2CNER), Kyushu University, 744 Motooka, Nishi, Fukuoka, Japan. [7]These authors contributed equally: Xiao-Chun Fan, Xun Tang. ✉e-mail: x-tang@opera.kyushu-u.ac.jp; wkai@suda.edu.cn; adachi@cstf.kyushu-u.ac.jp; xiaohong_zhang@suda.edu.cn

Nevertheless, device durability under continuous operation, which is highly dependent on charge carrier and exciton dynamics, remains the primary obstacle. Substantial efforts have been devoted to extending its longevity by optimizing the intrinsic properties of each component material. These efforts include reinforcing molecular rigidity to enhance photostability[13]; differentiating orbital angular momentum or incorporating heavy atoms to accelerate the triplet upconversion rate[14–16]; deuterium substitution to suppress high-frequency vibrations[17,18]; and constructing a sterically shielded structure to reduce detrimental Dexter energy transfer[19]. Unlike direct photon absorption under photoexcitation, the performance of electrically-driven devices is heavily associated with complicated charge carrier and exciton behaviours, *e.g.*, single carrier injection[20], transport[21], trapping[22,23], recombination[24,25], Förster/Dexter energy transfer[26], as well as multiple channels of exciton annihilations[27–29]. In blue OLEDs with wide energy gaps ($E_g > 2.6$ eV), the alignment of frontier molecular orbitals (FMOs) energy levels between adjacent layers plays a dominant role in determining the carrier dynamics and recombination pathways. For the representative blue MR prototypes like DABNA-2 and ν-DABNA, featuring single- and binary-boron units, respectively, their highest occupied molecular orbital (HOMO) levels are localized at around −5.4 eV[9,30]. These energy levels are much shallower than those of traditional blue phosphorescent or TADF emitters, as well as those of host matrices or assistant dopants (around −6.0 eV)[31], leading to significant carrier traps under electrical excitation. To gain a comprehensive view, the HOMO levels of the reported blue boron-containing MR emitters are summarized in Fig. 1a and Supplementary Table 1. It is evident that the HOMOs of most MR emitters are shallower than −5.6 eV, highlighting the dilemma of inadequate FMOs energy levels. Although given a few examples of blue MR emitters with HOMOs deeper than −5.6 eV, these studies primarily focused on structural modifications aimed at modulating photophysical properties, like reverse intersystem crossing process, emission wavelength, and spectral bandwidth[32,33]. Charge carrier trapping or blocking by inadequate energy levels has been found to impact device performance, while the underlying mechanism and effective strategies for adjusting the energy levels have not received sufficient attention[34,35].

In this work, we found that the energy levels of MR emitters at a low doping concentration (*i.e.*, 1 wt%) can significantly influence the charge carrier and exciton dynamics in devices. The shallow HOMO energy level of the blue MR prototype, CzDB ($E_{HOMO} = -5.32$ eV), induces severe hole trapping, which substantially hinders the charge carrier mobility, thus resulting in unideal current density–voltage (*J*–*V*) characteristics. Investigations into the transient delayed electroluminescent (EL) characteristics reveal that trapped charge carriers would affect the localization of the recombination zone. More importantly, these trapped carriers enable the determination of the

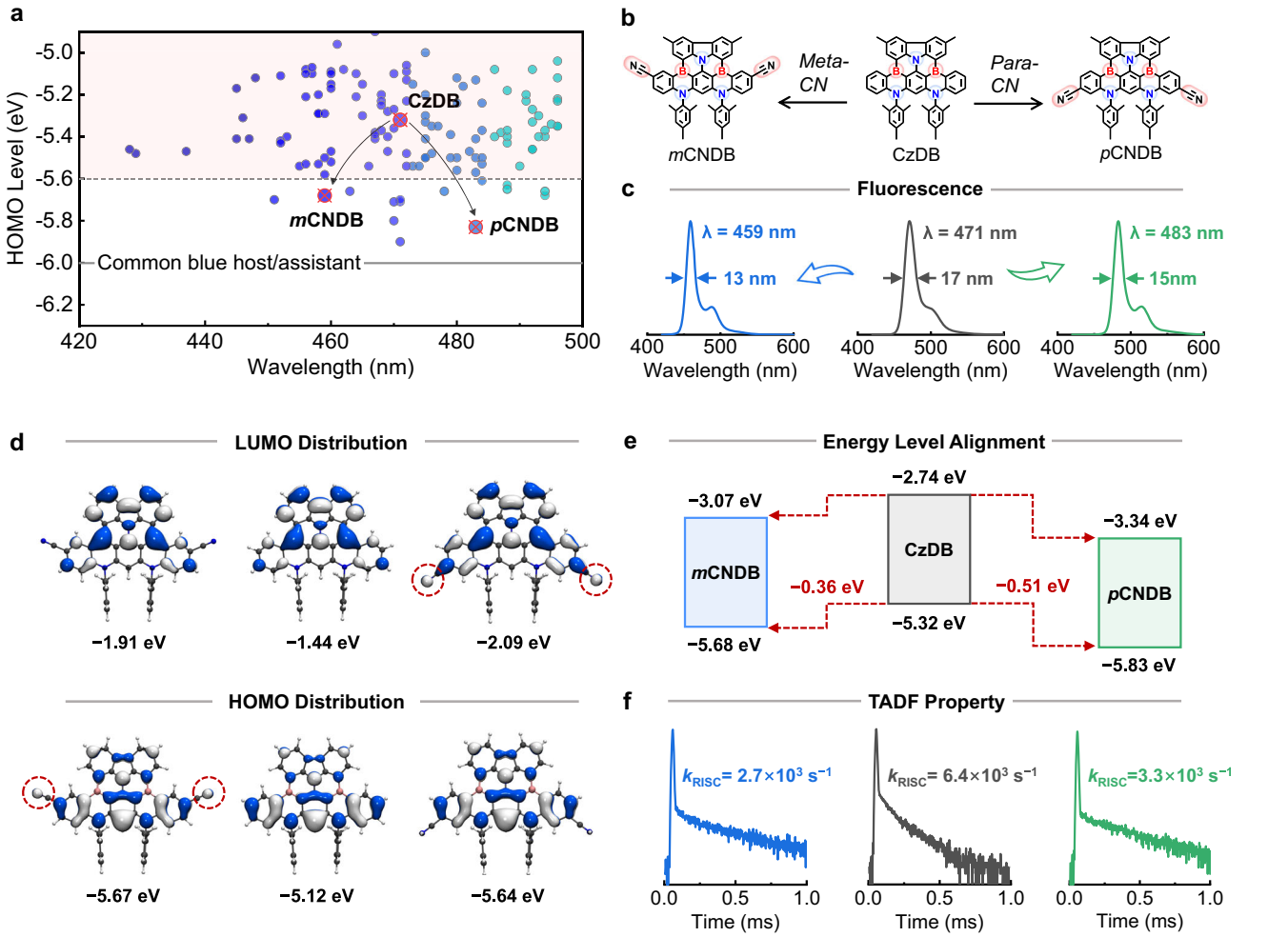


**Fig. 1 | Chemical structures, theoretical calculation, and photophysical properties of studied molecules. a** Summarized HOMO energy levels of reported blue boron-containing MR emitters. **b** Molecular design strategy and chemical structures. **c** Fluorescence spectra. **d** HOMO/LUMO distributions. **e** Experimental FMOs energy level alignments. **f** Transient PL decay curves of CzDB, *m*CNDB, and *p*CNDB in solution.

exciton generation pathway, indicating that excitons are prone to be directly formed at MR emitters rather than at assistant dopants or hosts in hyperfluorescent (HF) devices[26]. Consequently, the inadequate, shallow energy level of blue MR emitters accelerates device degradation. To address this issue, an effective strategy is proposed to modulate the FMO energy levels through wavefunction perturbation of the MR backbone. In specific, the electron-accepting cyano-groups are substituted at the peripheral positions of the MR backbone (CzDB). Due to the limited size of the cyano fragment, the wavefunction distribution in the molecular skeleton is not significantly reorganized, thus maintaining the dominance of the MR effect. This approach offers the advantages of (i) maintaining a narrow spectral bandwidth with high colour purity, and (ii) localizing the spectral wavelength to guarantee blue emission. Notably, although the photophysical properties of the modified molecules remain consistent with those of the pristine CzDB, the energy levels of the *meta*- and *para*-substituents, *m*CNDB ($E_{HOMO}$ = −5.68 eV) and *p*CNDB ($E_{HOMO}$ = −5.83 eV), are much deeper than that of CzDB ($E_{HOMO}$ = −5.32 eV). Consequently, the remarkable FMO energy level adjustment ($\Delta E_{HOMO}$ of 0.36 and 0.51 eV, respectively) leads to higher EQEs, reduced efficiency rolloff, and optimized operational stability in blue OLEDs.

## Results

### Molecular design and energy level tuning

As illustrated in Figs. 1b and 1c, double-boron-embedded CzDB is selected as the MR prototype because of its blue narrowband emission ($\lambda_{peak}$ = 471 nm, FWHM = 17 nm)[36]. The structural and electronic properties of CzDB were initially investigated using density functional theory (DFT) and time-dependent DFT (TD-DFT) calculations at the PEB0/6-31 G(d,p) level (Fig. 1d). As expected, HOMO and the lowest unoccupied molecular orbital (LUMO) wavefunctions are mainly distributed at the discrete nitrogen and boron atoms, resulting in short-distance MR effect within the robust skeleton, *i.e.*, narrowband emission. Moreover, the atomic HOMO/LUMO separation induces a small experimental singlet-triplet splitting ($\Delta E_{ST}$ = 0.11 eV), triggering the TADF property (Supplementary Fig. 1). However, the simulated low-lying HOMO level of CzDB is localized at −5.12 eV, which is consistent with traditional MR molecules (summarized in Fig. 1a and Supplementary Table 1). To resolve this dilemma, electron-accepting cyano motifs are employed to substitute at the *meta*- and *para*-positions of the central boron atoms in the periphery BN backbone. As depicted in Fig. 1d and Supplementary Fig. 2, the simulation suggests that the limited size of the cyano fragments would barely influence the molecular rigidity and the wavefunction distribution at the BN core. Thus, the MR effect still governs the electronic properties of both *m*CNDB and *p*CNDB. These molecules exhibit an extremely small root mean square displacement (RMSD) of around 0.030 Å between the optimized singlet excited state ($S_1$) and ground state ($S_0$) configurations, indicating negligible structural relaxation under the excited state with cyano substituents. Furthermore, Huang–Rhys (HR) factors for the $S_1 \rightarrow S_0$ transition are calculated. The dominant vibration modes of these molecules are primarily from the out-of-plane distortion of the CzDB core at low frequency, whereas cyano units barely contribute to the structural vibrations (Supplementary Fig. 3). As a result, the spectral widths of both *m*CNDB and *p*CNDB are as narrow as 13 and 15 nm, respectively, preserving the high colour purity in pure blue (459 nm) to sky blue (483 nm) emission (Supplementary Fig. 4). Gaining deeper insight into the function of cyano-units, the varying substitution positions lead to different effects on their electronic characteristics. In *m*CNDB, cyano is localized at the *meta*-position of boron, as well as the *para*-position of nitrogen, primarily contributing to the HOMO distribution. Thus, this weakens the electron-donating ability of the skeleton, resulting in a deeper HOMO level (−5.67 eV) than that of the pristine CzDB (−5.12 eV). In contrast, incorporating the cyano unit in *p*CNDB enhances the conjugation coupling with the *para*-B atoms, thus mainly participating in the LUMO distribution. The reinforced electron-accepting strength induces a much deeper LUMO level (−2.09 eV) than that of CzDB (−1.44 eV), along with a deeper HOMO level (−5.64 eV), due to the electronic effect in the highly conjugated molecular system[37]. Noteworthy, despite the significant shifts in their HOMO/LUMO levels, wide bandgaps of 3.68, 3.76, and 3.55 eV are reserved for CzDB, *m*CNDB, and *p*CNDB, respectively, with narrowband blue luminescence. To validate the accuracy of the simulated HOMO/LUMO energy levels, cyclic voltammetry (CV) and ultraviolet photoelectron spectroscopy were used to measure the energy levels in the solution and the solid state, respectively (Supplementary Figs. 5–7). The HOMO levels of CzDB, *m*CNDB, and *p*CNDB are determined to be −5.32, −5.68, and −5.83 eV, respectively, which are consistent with the prediction of the DFT calculation.

The photophysical characteristics of CzDB, *m*CNDB, and *p*CNDB in solid-state films are successively investigated. The blend films are composed of 1.5 wt% emitters in a 3,3′ -bis(carbazol-9-yl)biphenyl (mCBP) host matrix. The photoluminescent quantum yields (PLQYs) of the *m*CNDB- and *p*CNDB-based films are 86% and 89%, respectively, which are slightly higher than that of the CzDB-based film (85%). Furthermore, distinct delayed components are observed in these blend films from the transient PL decay profiles, confirming the TADF nature of the three emitters (Supplementary Figs. 8 and 9). In specific, the larger $\Delta E_{ST}$ values of *m*CNDB (0.16 eV) and *p*CNDB (0.15 eV) than that of CzDB (0.10 eV) in the solid-state films (Supplementary Fig. 10), which is consistent with the singlet-triplet energy difference measured in toluene. It can be partially explained by a larger wavefunction overlap integral (0.53, 0.57, and 0.60 for CzDB, *m*CNDB, and *p*CNDB, respectively) after incorporating cyano-units. Therefore, the reverse intersystem crossing (RISC) rates of the *m*CNDB- and *p*CNDB-based films ($2.7 \times 10^3$ and $3.3 \times 10^3\,s^{-1}$, respectively) are slightly slower than that of the CzDB-based film ($6.4 \times 10^3\,s^{-1}$). Additionally, the photostability of the three molecules in a degassed toluene solution was evaluated. The comparable PL intensity degradation under a constant excitation power of 5 mW $cm^{-2}$ indicates that the incorporation of cyano units barely affects the molecular stability (Supplementary Fig. 11). The detailed photophysical data of the three molecules are summarized in Supplementary Table 2. Although the photophysical characteristics of *m*CNDB and *p*CNDB are comparable to those of CzDB, their energy level variation would sufficiently influence the electrical properties.

### Charge carrier dynamics in non-sensitized OLEDs

To evaluate the impact of varied energy levels on their EL properties, OLEDs incorporating a emitting layer (EML) with the host-guest system are fabricated as the following architecture (Supplementary Fig. 12): indium tin oxide (ITO), 1,4,5,8,9,11-hexaazatriphenylene hexacarbonitrile (HAT-CN, 10 nm), $N^4$,$N^{4'}$-di(naphthalen-1-yl)-$N^4$,$N^{4'}$-diphenyl-[1,1′-biphenyl]−4,4′-diamine (NPD, 20 nm), 9-phenyl-3,6-bis(9-phenyl-9H-carbazol-3-yl)−9H-carbazole (Tris-PCz, 10 nm), mCBP (5 nm), 1.5 wt% emitters: mCBP (30 nm), SF3-TRZ (10 nm), 30 wt% 8-quinolinolato lithium (Liq): SF3-TRZ (30 nm), Liq (2 nm), and aluminium (Al, 100 nm). Specifically, mCBP is employed as the electron-blocking layer and host matrices, which governs the dynamic behaviours of charge carriers. Moreover, the adjacent SF3-TRZ serves as the hole-blocking layer, which dominates electron injection. The HOMO and LUMO levels of the compounds in the charge carrier blocking layers and EML are illustrated in Fig. 2a. The characteristics of current density-driving voltage-luminance (*J-V-L*) are exhibited in Fig. 2d. In contrast of *m*CNDB- and *p*CNDB-based OLEDs, the CzDB-based device demands a much larger driving voltage. Noticeably, HOMO/LUMO levels (−5.32/−2.74 eV) of CzDB are much shallower than those of either *m*CNDB (−5.68 and −3.07 eV) or *p*CNDB (−5.83 and −3.34 eV), which are responsible for the electrical properties. To clarify the mechanism of different *J-V* characteristics, electron-only and hole-only devices (EOD and HOD) are

https://doi.org/10.1038/s41467-025-60172-y

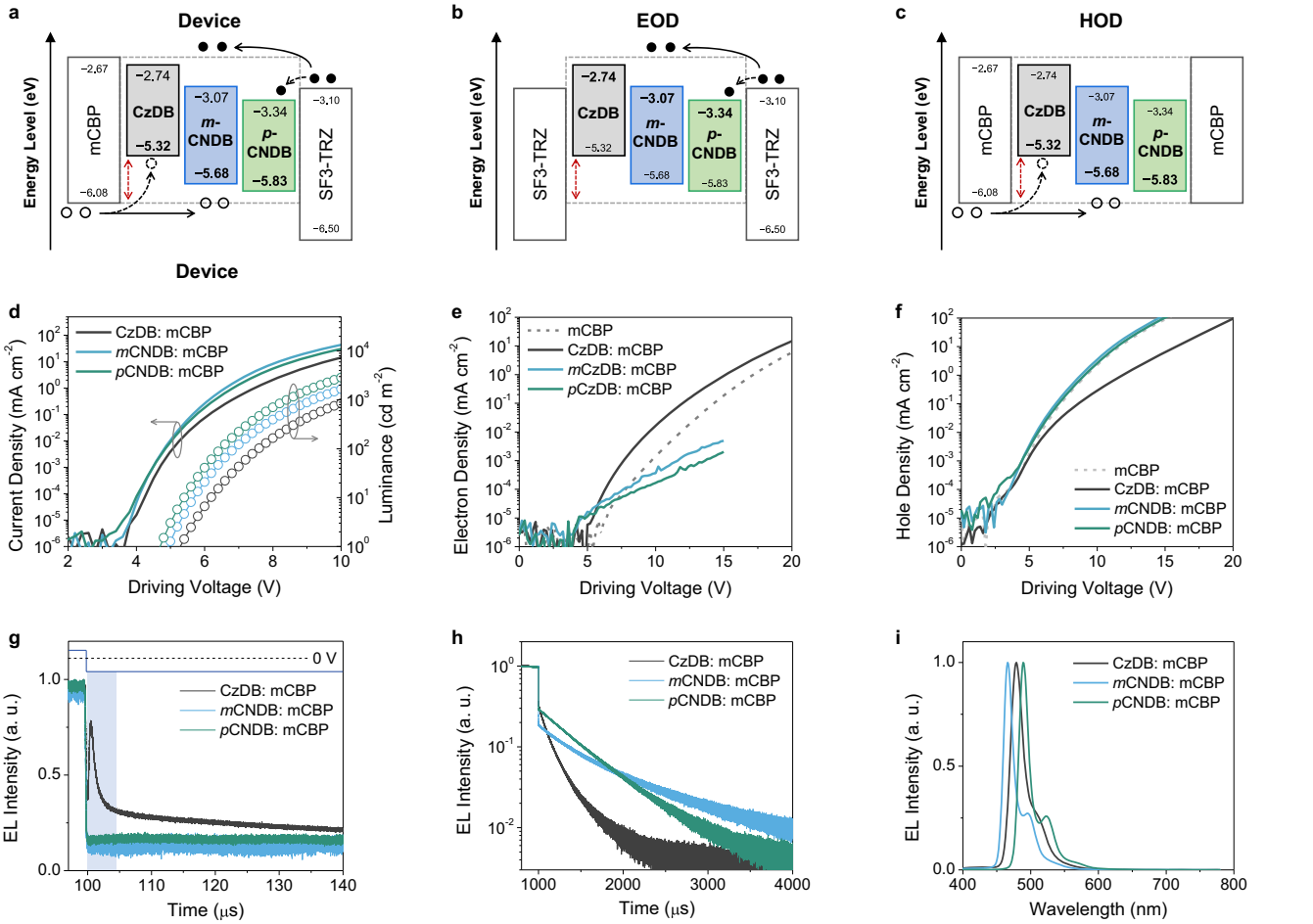


**Fig. 2 | Device performance and charge carrier dynamic of non-sensitized OLEDs.** Energy level alignment of EBL/EML/HBL in (**a**) OLED, (**b**) EOD, and **c** HOD based on 1.5 wt% CzDB, *m*CNDB, and *p*CNDB doped in mCBP blend films. Current density-to-driving voltage curves for (**d**) OLED, (**e**) EOD, and (**f**) HOD based on 1.5 wt% CzDB, *m*CNDB, and *p*CNDB doped into mCBP blend films. **g** Transient EL decay characteristics after applying a reverse bias voltage of −10 V. **h** Transient EL delayed components after switching off the driving voltage. **i** EL spectra of the corresponding OLEDs at 1000 cd $m^{-2}$.

respectively designed to independently reveal the single charge carrier dynamics under electrical excitation without the hole-electron recombination process (Fig. 2b, c, and Methods). At the electron side, LUMO levels of SF3-TRZ and the adjacent mCBP matrix were reported to be −3.10 and −2.74 eV, respectively, leading to a distinct energy gap (0.36 eV) for insufficient electron injection[21]. Consequently, EOD based on the mCBP neat film exhibits a large electron injection voltage ($V_{ei}$, ~5.5 V) and poor electron transport, as shown in Fig. 2e. After doping 1.5 wt% CzDB in mCBP matrix, the $V_{ei}$ (~5.0 V) is slightly reduced, and the electron transport capability is enhanced. In contrast, *m*CNDB- and *p*CNDB-based EODs show the opposite characteristic of a reduced $V_{ei}$ (~3.0 V), while a much poorer electron flow upon increasing the driving voltage. The variation in EODs can be ascribed to the LUMO alignment of the CzDB derivatives, where the LUMO levels of *m*CNDB (−3.07 eV) and *p*CNDB (−3.34 eV) are equivalent to that of SF3-TRZ ( −3.10 eV), leading to a non-barrier electron injection. Conversely, CzDB, with a shallow LUMO (−2.74 eV), is close to mCBP, maintaining a relatively large energy gap with SF3-TRZ. In addition, HOD undergoes different dynamic behaviours (Fig. 2c and f). Either *m*CNDB- or *p*CNDB-based HODs have an identical *J-V* property to that of mCBP-based HOD, suggesting the hole transport is governed by mCBP matrices. However, the CzDB-based HOD shows much-suppressed hole transport, as shown in Fig. 2f. Notably, CzDB has the shallowest LUMO level of −5.32 eV, and the substantial energy gap ($\Delta E_{HOMO}$ = 0.76 eV) with mCBP makes it act as the deep wells to trap the mobile holes. Upon applying a reverse bias voltage (−10 V) after switching off the pulsed EL excitation (pulse width of 100 μs), an intense EL spike appears in the CzDB-based OLED, indicating the hole trapping effect in CzDB molecules with shallow energy levels (Fig. 2g)[38,39].

Furthermore, the varied charge carrier dynamics alter exciton generation and recombination. To accurately determine the recombination zone, a deep-red emitter, bis(1-phenylisoquinoline)(acetylacetonate)iridium(III) [$Ir(piq)_2acac$], is used as an indicator for the exciton density at different positions (5, 15, 25, and 30 nm) in the EML. The thickness of $Ir(piq)_2acac$ is controlled at 0.3 nm to eliminate the effect on charge carrier transport. As shown in Supplementary Fig. 13, the deep-red spectra from $Ir(piq)_2acac$ with the wavelength maximal at 635 nm is proportional to the probability of charge carrier recombination. Therefore, it is found that the recombination zone of *m*CNDB- and *p*CNDB-based OLEDs is primarily localized at the EML/SF3-TRZ interface (between positions 4 and 3). Instead, an extensive shift of the recombination zone to the hole injection side occurs in the CzDB-based device. Moreover, it becomes broader from positions 1 to 3, indicating that trapped single carriers can affect the distribution of the recombination zone. Although EQEs exceeding 10% are achieved for both *m*CNDB- and *p*CNDB-based OLEDs operating at a low current density (<$10^{-2}$ mA $cm^{-2}$), severe efficiency rolloff takes place because of their long triplet lifetime (~500 μs, Fig. 2h) and the associated exciton annihilation when increasing the current density (Supplementary Fig. 14). Particularly, *m*CNDB- and *p*CNDB-based OLEDs show narrowband spectra with FWHMs of 17 nm at pure-blue (466 nm) and sky-blue (489 nm) regimes.

### Charge carrier dynamics in hyperfluorescent (HF) OLEDs

To further enhance the device performance, a sky-blue TADF assistant HDT-1 is utilized to construct the hyperfluorescent (HF) system[40]. The doping concentration of HDT-1 is controlled at 20 wt%, which would remarkably affect the charge carrier dynamics in the devices (Fig. 3). HOMO and LUMO levels of HDT-1 are measured at −5.98 and −3.31 eV, respectively (Supplementary Fig. 15). Initially, HOD based on a 20 wt% HDT-1: mCBP blend film is fabricated, and the *J*–*V* curve is identical to that of the mCBP-based HOD, indicating that the HDT-1 dopant does not affect the hole injection and transport capabilities (Fig. 3a, d). As expected, since the HOMO level of HDT-1 is as deep as that of the mCBP host matrix, the hole injection and transport characteristics of the corresponding HF devices, after doping 1.5 wt% *m*CNDB and *p*CNDB with relatively deeper HOMO levels, are identical to those of the host-guest devices (Fig. 3a, d). Notably, the hole flow in the CzDB-based HF HOD remains hindered, which is attributed to the significant HOMO gap (0.66 eV) between CzDB and HDT-1. In contrast, the electron dynamics undergo substantial changes. As HDT-1 has a much higher doping concentration (20 wt%) and a deeper LUMO level (−3.31 eV) than SF3-TRZ (−3.10 eV, Fig. 4b), electron injection from SF3-TRZ to the EML becomes easier, thus reducing the corresponding $V_{ei}$ to 2.0 V. Particularly, the electron flow density is inversely proportional to the LUMO gap between the emitters and HDT-1. Thus, *m*CNDB- and *p*CNDB-based HF EODs with smaller LUMO gaps ($\Delta E_{LUMO}$ = 0.24 and 0.03 eV) exhibit optimized electron transport, whereas CzDB-based HF EOD demonstrates slightly poor electron transport because of its large $\Delta E_{LUMO}$ of 0.57 eV. Subsequently, the corresponding HF OLEDs are fabricated. As anticipated, the CzDB-based HF device still exhibits a worse *J*–*V*–*L* characteristic due to the hole-trapping effect, which can be confirmed by a transient EL spike after applying the reverse bias (−10 V, Fig. 3g) to the device. In addition, the impedance spectroscopy indicates that the trapped charge carriers in CzDB dopants in the HF device notably results in a much higher recombination resistance than that of *m*CNDB- and *p*CNDB-based HF devices (Supplementary Fig. 16), highlighting the effect by the FMO energy level alignment. The EL spectra of HF OLEDs are demonstrated in Fig. 3h, with emission peaks at 478 nm (CzDB-based), 466 nm (*m*CNDB-based), and 489 nm (*p*CNDB-based), ranging from pure-blue to sky-blue. Additionally, narrow FWHMs of around 20 nm are obtained in these devices. Benefiting from the more balanced carriers, *m*CNDB- and *p*CNDB-based HF OLEDs exhibit maximum EQEs exceeding 23% while maintaining around 20% at a high luminance of 1000 cd m$^{-2}$ (Fig. 3i). By comparison, a lower maximum EQE of 20% is observed in the CzDB-based HF OLED, accompanied by more severe efficiency rolloff (24.8%) at 1000 cd m$^{-2}$, which is larger than those (19.3% and 12.9%) of *m*CNDB- and *p*CNDB-based HF devices (Supplementary Table 3).

### Exciton generation and recombination

As the performance variation of the HF devices is based on CzDB and its derivatives, it is suggested that charge carrier trapping significantly alters the exciton generation and recombination process. The incorporation of HDT-1 results in a significant change in the electron injection and transport properties, which subsequently influences the exciton recombination behaviours. Similar to the host-guest devices,

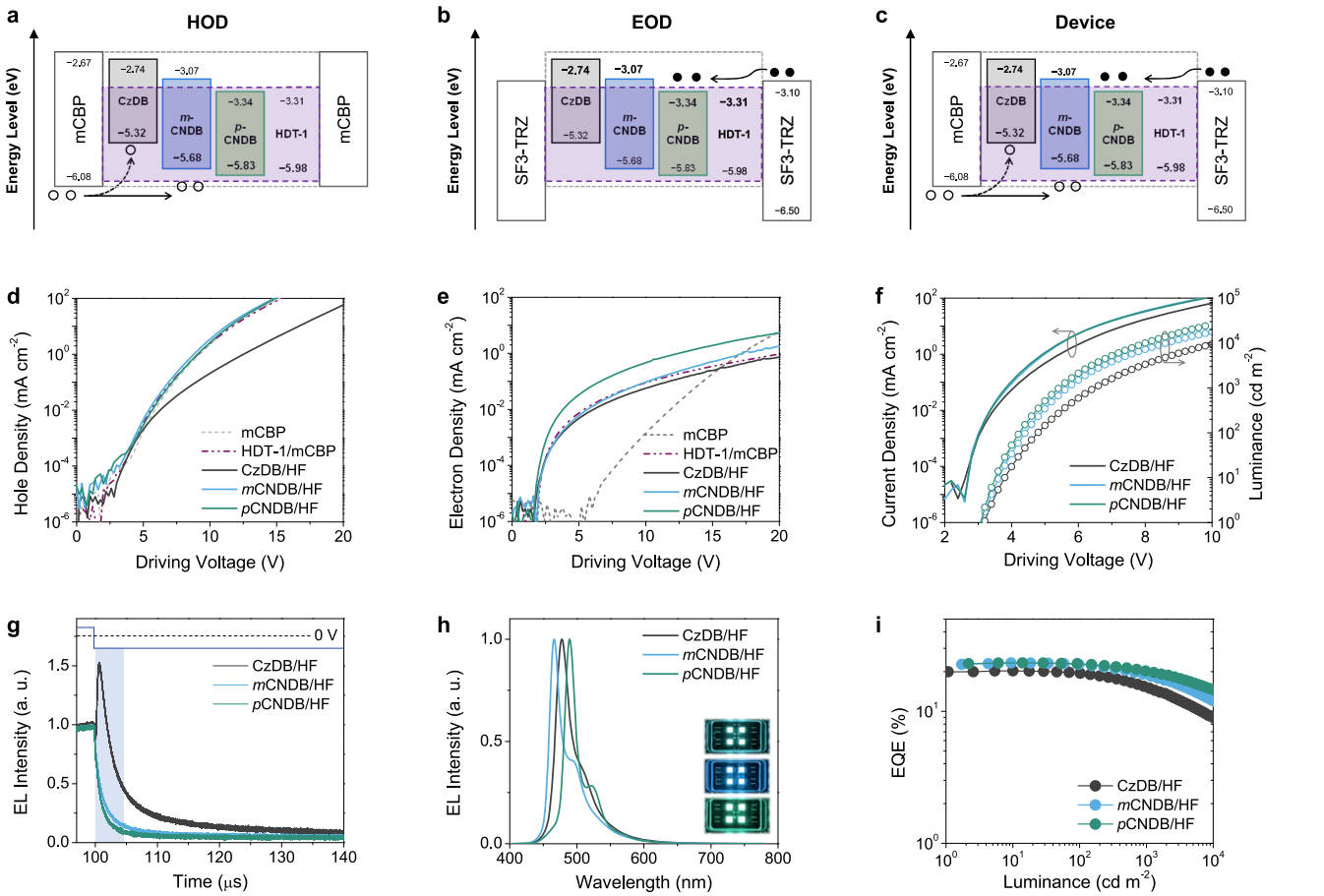


**Fig. 3 | Device performance and charge carrier dynamic of HF OLEDs.** Energy level alignment of EBL/EML/HBL in (**a**) HOD, (**b**) EOD, and (**c**) HOD based on CzDB, *m*CNDB, and *p*CNDB doped in HF (HDT-1: mCBP) blend films. Current density-to-driving voltage curves for (**d**) OLED, (**e**) EOD, and (**f**) HOD based on CzDB, *m*CNDB, and *p*CNDB doped in HF (HDT-1: mCBP) blend films. **g** Transient EL decay characteristics after applying the reverse bias voltage. **h**. EL spectra of the corresponding HF OLEDs. **i** EQE–current density curve for HF devices. The insets are photographs of the operating OLEDs at 1000 cd m$^{-2}$.

https://doi.org/10.1038/s41467-025-60172-y

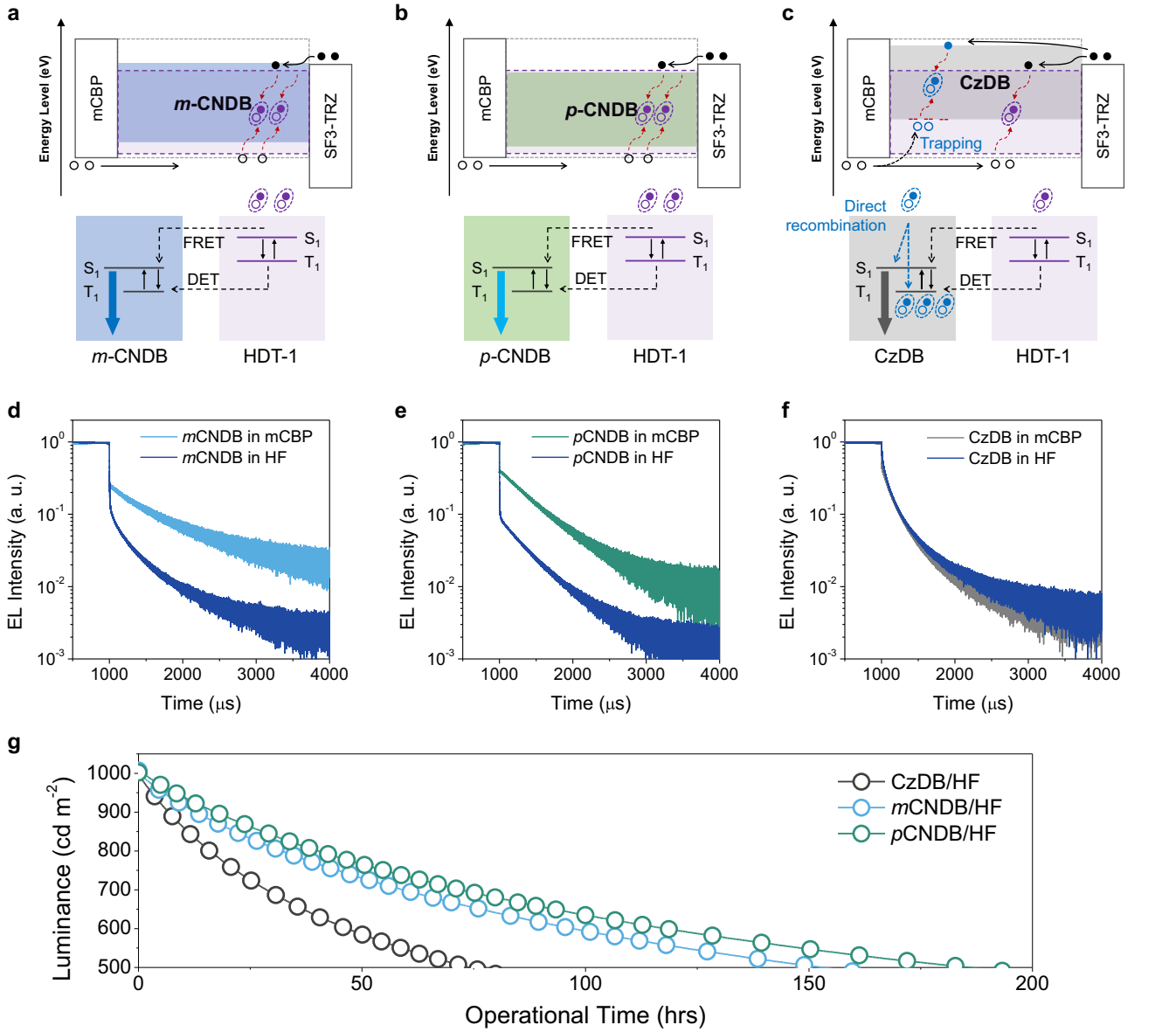


**Fig. 4 | Exciton dynamic and operational lifetime of HF OLEDs.** Illustration of the exciton generation and energy transfer processes in (**a**) CzDB-, (**b**) *m*CNDB-, and (**c**) *p*CNDB-based HF devices (the doping concentrations of emitter and HDT-1 are 1.5 and 20 wt%, respectively). Transient EL delayed emission properties of host-guest and HF OLEDs based on (**d**) CzDB-, (**e**) *m*CNDB-, and (**f**) *p*CNDB. (**g**) Operational EL stability of CzDB-, *m*CNDB-, and *p*CNDB-based HF OLEDs. The initial luminance is 1000 cd $m^{-2}$.

the recombination zone distribution in HF devices is experimentally determined by inserting an ultra-thin layer (0.3 nm) of a deep red indicator [$Ir(piq)_2acac$] at different positions (5, 15, 25, and 30 nm) in the EML of the HF devices. As illustrated in Supplementary Fig. 17, at a low current density (~0.01 mA $cm^{-2}$), the maximal probability of exciton recombination in all HF OLEDs occurs at the EBL/EML interface, which is consistent with the enhanced electron injection and transporting capability in EODs. However, as the current density increases to 1 mA $cm^{-2}$, the recombination zone of *m*CNDB- and *p*CNDB-based HF OLEDs shifts toward the SF3-TRZ side due to the reduced electron transport. Despite the worse electron transport capability in CzDB-based HF devices than in *m*CNDB- and *p*CNDB-based HF devices, the drift of its recombination zone to the electron injection side is slower. In other words, the exciton density at positions 1 and 2 remains dominant. Combined with the fixed recombination zone distribution in the CzDB-based host–guest device, these abnormal characteristics indicate that the shallow HOMO level not only blocks charge carrier migration but also affects the exciton generation pathways. As illustrated in Fig. 4a–c, in the cases of *m*CNDB and *p*CNDB with deeper HOMO energy levels, exciton generation in the corresponding HF devices is primarily localized at HDT-1 molecules, followed by sufficient Förster resonant energy transfer (FRET) to the terminal emitters for radiation. In contrast, the trapped holes are expected to induce direct exciton formation at CzDB molecules with a shallow HOMO level instead of the HDT-1 assistant dopants. To verify this hypothesis, systematic investigations into the transient EL delayed characteristics of OLEDs based on CzDB, *m*CNDB, and *p*CNDB are conducted. As can be seen in Fig. 4d–f, the delayed emissive components of both *m*CNDB- and *p*CNDB-based HF devices are much smaller than those of their host-guest devices, indicating that a large proportion of excitons are generated at the HDT-1 molecules, whereas the reduced proportion of triplets at *m*CNDB and *p*CNDB is attributed to the Dexter energy transfer from the triplet state of HDT-1. In contrast, the HF OLED based on CzDB with a shallow HOMO energy level exhibits different

characteristics. The delayed emissive component of the HF device is identical to that of its host-guest OLED (Fig. 4f), demonstrating direct exciton generation at the terminal emitters rather than the HDT-1 sensitizers. Therefore, the increased density of long-lived triplets at CzDB molecules is likely to cause exciton quenching, which is consistent with its lower EQE and more severe efficiency rolloff compared to *m*CNDB- and *p*CNDB-based HF devices. More importantly, direct exciton generation at the terminal emitters is detrimental to the device durability. As a result, although these three molecules possess equivalent photostability and FRET efficiency ($5\times10^6\ s^{-1}$) in HF blend films (Supplementary Fig. 18-20. Table 4), pure-blue *m*CNDB- and sky-blue *p*CNDB-based HF OLEDs exhibit much optimized operational EL stability (Fig. 4g) with exceeding two-fold enhancement under a high luminance of 1000 cd $m^{-2}$, highlighting the importance of precious energy level modulation for achieving highly stable blue OLEDs.

## Discussion

Numerous efforts have been made to stabilize blue OLEDs. In particular, in advanced HF systems, excitons are expected to initially generate efficient phosphors or TADF sensitizers to manage triplet excitons. Therefore, optimizing the intrinsic photophysical properties of phosphors, TADF assistant dopants, and terminal emitters, such as increasing their triplet energy levels, reinforcing their molecular stability, and accelerating the triplet upconversion rate, has become mainstream. However, unlike photoexcitation, the pathways for exciton formation under electrical excitation are critical yet often overlooked.

This work demonstrated that charge carrier trapping by terminal emitters significantly impacts the charge carrier mobility and determines the pathways of exciton generation. A blue MR molecule, CzDB, with a shallow energy level ($E_{HOMO}$ = −5.32 eV), is chosen as the prototype because its distinct delayed lifetime difference from that of HDT-1 makes it easier to distinguish the sources of the delayed components. In CzDB-based HF devices, it is concluded that the free charge carriers would directly recombine at the terminal emitters rather than the TADF sensitizers, resulting in unsatisfactory device performance. To resolve this issue, a strategy of wavefunction perturbation in blue MR backbones is proposed. The incorporation of electron-withdrawing cyano units maintains the narrowband blue emission (FWHM = 13 and 15 nm, respectively) while substantially deepening the HOMO/LUMO levels (−5.68 and −5.83 eV, respectively). Consequently, severe hole trapping and direct exciton recombination issues caused by MR emitters are circumvented, leading to a higher EQE exceeding 23%, a suppressed efficiency rolloff, and optimized operational durability in blue OLEDs.

As discussed, the prototype molecule CzDB that we chose is aimed at clarifying the pathways of exciton generation and recombination. However, its intrinsic limitations, like a slow RISC rate (~$10^3\ s^{-1}$), imped the realization of the high performance. Given that the energy levels of MR molecules are generally shallow (Fig. 1a), charge carrier trapping-induced drawbacks prevalently occur in the corresponding devices. Thus, we believe that the wavefunction perturbation strategy enables us to feasibly modulate the energy levels of other advanced MR platforms, such as ν-DABNA[9], V-DABNA[41], and ω-DABNA[42], to advance state-of-the-art blue OLEDs.

## Methods

### Material

All reagents were purchased from commercial sources and used without further purification (Supplementary Fig. 21). $^1$H NMR and $^{13}$C NMR spectra were recorded on a Bruker 400/101 MHz spectrometer in deuterium reagent at room temperature. MALDI-TOF mass data were recorded on a Bruker ultrafleXtreme instrument. High-resolution mass spectrometry (HRMS) data were recorded on Thermo Scientific QE plus (Supplementary Figs 22–27).

### Photophysical measurement

UV–vis absorption spectra were recorded on a Hitachi U-3900 spectrophotometer. Photoluminescence (PL) spectra were recorded on a Hitachi F-4600 fluorescence spectrophotometer. Transient PL decays were measured on an integrated streak camera system (C4334, Hamamatsu Photonics). The absolute PLQY was recorded on a Hamamatsu Quantaurus-QY quantum yield spectrometer (C13534-11). The angle-dependent PL spectra of the doped films were measured via a molecular orientation characteristic measurement system (C14234-11, Hamamatsu Photonics). The photostability in solution was estimated by using a multichannel spectrometer (PMA-12, Hamamatsu Photonics) under 300–400 nm light (5 mW $cm^{-2}$) irradiation via xenon light (MAX-303, Asahi Spectra) with a UV light intensity feedback control unit. The photostability of the HF blend films was measured in a nitrogen atmosphere by using a multichannel analyser (C14631, Hamamatsu Photonics, Japan) under 300–400 nm light (25 mW $cm^{-2}$) irradiation from a filtered Xe lamp (MAX-350, Asahi Spectra, Japan).

### Energy level measurements

The highest occupied molecular orbital (HOMO) energy levels of the emitters in the films were determined by atmospheric ultraviolet photoelectron spectroscopy using a photoelectron emission spectrometer (Riken Keiki AC-3). Cyclic voltammetry (CV) curves were recorded on a CHI660e electrochemistry station in an oxygen-free dichloromethane (DCM) solution with tetrabutylammonium hexafluorophosphate ($Bu_4NPF_6$) at a scan rate of 0.1 V $s^{-1}$.

### Theoretical calculation

All calculations were performed with the Gaussian 16 programme package[43]. The equilibrium geometry of the ground state was determined by density functional theory (DFT) using the PBE0 density functional method with a basis set of 6-31 G(d,p). The Huang–Rhys (HR) factors for the $S_1 \rightarrow S_0$ transition were determined with the DUSHIN module in MOMAP (Molecular Materials Property Prediction Package)[44]. All calculations were performed in the gas phase. The molecular structure, frontier molecular orbital, and electron distribution models were rendered by Multiwfn and VMD[45,46].

### Hole-only and electron-only devices (HODs and EODs)

Hole-only device structure: ITO/HAT-CN (10 nm)/NPD (20 nm)/TrisPCz (10 nm)/mCBP (5 nm)/EML (50 nm)/mCBP (5 nm)/TrisPCz (10 nm)/NPD (20 nm)/HAT-CN (10 nm)/Al (100 nm). Electron-only device structure: ITO/Liq (2 nm)/SF3-TRZ: Liq (30 wt%, 30 nm)/SF3-TRZ (10 nm)/EML (50 nm)/SF3-TRZ (10 nm)/SF3-TRZ: Liq (30 wt%, 30 nm)/Liq (2 nm)/Al (100 nm).

### Device characterization

The electrical characteristics of the devices were measured using a source metre (Keysight B2911A, Keysight Technologies) and a luminance metre (CS-2000, Konica Minolta, Japan). The lifetimes of all devices are measured using a luminance metre (SR-3AR, TOPCON, Japan) under constant current density driving conditions with an initial luminance of 1000 cd $m^{-2}$.

### Transient electroluminescent (EL) radiation measurements

Pulsed voltages were applied by using a function generator, the light signals were detected via a photomultiplier tube (PMT) module (H10721-01, Hamamatsu Photonics, Japan), and the current signals from the PMT were amplified using a current amplifier (DHPCA-100, Femto, Germany).

## Data availability

The data that support the findings of this study are available in the supplementary material of this article. Source data are provided in this paper. Source data are provided with this paper.

## References


1. Tang, C. W. & Vanslyke, S. A. Organic electroluminescent diodes. *Appl. Phys. Lett.* **51**, 913–915 (1987).
2. Baldo, M. A., O'Brien, D. F., You, Y., Shoustikov, A., Sibley, S., Thompson, M. E. & Forrest, S. R. Highly efficient phosphorescent emission from organic electroluminescent devices. *Nature* **395**, 151–154 (1998).
3. Uoyama, H., Goushi, K., Shizu, K., Nomura, H. & Adachi, C. Highly efficient organic light-emitting diodes from delayed fluorescence. *Nature* **492**, 234–238 (2012).
4. Xu, Y., Xu, P., Hu, D. & Ma, Y. Recent progress in hot exciton materials for organic light-emitting diodes. *Chem. Soc. Rev.* **50**, 1030–1069 (2021).
5. Cui, L.-S. et al. Fast spin-flip enables efficient and stable organic electroluminescence from charge-transfer states. *Nat. Photon.* **14**, 636–642 (2020).
6. Tang, X. et al. Highly efficient luminescence from space-confined charge-transfer emitters. *Nat. Mater.* **19**, 1332–1338 (2020).
7. Wada, Y., Nakagawa, H., Matsumoto, S., Wakisaka, Y. & Kaji, H. Organic light emitters exhibiting very fast reverse intersystem crossing. *Nat. Photon.* **14**, 643–649 (2020).
8. Meng, G. et al. High-efficiency and stable short-delayed fluorescence emitters with hybrid long- and short-range charge-transfer excitations. *Nat. Commun.* **14**, 2394 (2023).
9. Kondo, Y. et al. Narrowband deep-blue organic light-emitting diode featuring an organoboron-based emitter. *Nat. Photon.* **13**, 678–683 (2019).
10. Mamada, M., Hayakawa, M., Ochi, J. & Hatakeyama, T. Organoboron-based multiple-resonance emitters: synthesis, structure-property correlations, and prospects. *Chem. Soc. Rev.* **53**, 1624–1692 (2024).
11. Kim, H. J. & Yasuda, T. Narrowband emissive thermally activated delayed fluorescence materials. *Adv. Opt. Mater.* **10**, 2201714 (2022).
12. Oda, S. et al. Development of pure green thermally activated delayed fluorescence material by cyano substitution. *Adv. Mater.* **34**, 2201778 (2022).
13. Wang, X. et al. Improving the stability and color purity of a BT.2020 blue multiresonance emitter by alleviating hydrogen repulsion. *Sci. Adv.* **9**, eadh1434 (2023).
14. Hu, Y. X. et al. Efficient selenium-integrated TADF OLEDs with reduced roll-off. *Nat. Photon.* **16**, 803–810 (2022).
15. Fan, X. C. et al. Ultrapure green organic light-emitting diodes based on highly distorted fused π-conjugated molecular design. *Nat. Photon.* **17**, 280–285 (2023).
16. Cheon, H. J., Woo, S. J., Baek, S. H., Lee, J. H. & Kim, Y. H. Dense local triplet states and steric shielding of a multi-resonance TADF emitter enable high-performance deep-blue OLEDs. *Adv. Mater.* **34**, e2207416 (2022).
17. Jung, S. et al. Enhancing operational stability of OLEDs based on subatomic modified thermally activated delayed fluorescence compounds. *Nat. Commun.* **14**, 6481 (2023).
18. Huang, T. et al. Enhancing the efficiency and stability of blue thermally activated delayed fluorescence emitters by perdeuteration. *Nat. Photon.* **18**, 516–523 (2024).
19. Cho, H. H. et al. Suppression of Dexter transfer by covalent encapsulation for efficient matrix-free narrowband deep blue hyperfluorescent OLEDs. *Nat. Mater.* **23**, 519–526 (2024).
20. Kotadiya, N. B. et al. Universal strategy for Ohmic hole injection into organic semiconductors with high ionization energies. *Nat. Mater.* **17**, 329–334 (2018).
21. Cui, L. S. et al. Long-lived efficient delayed fluorescence organic light-emitting diodes using n-type hosts. *Nat. Commun.* **8**, 2250 (2017).
22. Shockley, W. The Theory of p-n Junctions in Semiconductors and p-n Junction Transistors. *Bell Syst. Tech.* **28**, 435–489 (1949).
23. Kotadiya, N. B., Mondal, A., Blom, P. W. M., Andrienko, D. & Wetzelaer, G. A. H. A window to trap-free charge transport in organic semiconducting thin films. *Nat. Mater.* **18**, 1182–1186 (2019).
24. Regnat, M., Pernstich, K. P. & Ruhstaller, B. Influence of the bias-dependent emission zone on exciton quenching and OLED efficiency. *Org. Electron.* **70**, 219–226 (2019).
25. Wetzelaer, G. J. A. H., Kuik, M. & Blom, P. W. M. Identifying the nature of charge recombination in organic solar cells from charge-transfer state electroluminescence. *Adv. Energy Mater.* **2**, 1232–1237 (2012).
26. Stavrou, K., Franca, L. G., Danos, A. & Monkman, A. P. Key requirements for ultraefficient sensitization in hyperfluorescence organic light-emitting diodes. *Nat. Photon.* **18**, 554–561 (2024).
27. Song, W., Kim, T., Lee, J. Y., Lee, Y. & Jeong, H. Investigation of degradation mechanism of phosphorescent and thermally activated delayed fluorescent organic light-emitting diodes through doping concentration dependence of lifetime. *J. Ind. Eng. Chem.* **68**, 350–354 (2018).
28. Kondakov, D. Y. Triplet-triplet annihilation in highly efficient fluorescent organic light-emitting diodes: current state and future outlook. *Philos. Trans. R. Soc. A* **373**, 20140321 (2015).
29. Giebink, N. C. et al. Intrinsic luminance loss in phosphorescent small-molecule organic light emitting devices due to bimolecular annihilation reactions. *J. Appl. Phys.* **103**, 044509 (2008).
30. Hatakeyama, T. et al. Ultrapure blue thermally activated delayed fluorescence molecules: Efficient HOMO-LUMO separation by the multiple resonance effect. *Adv. Mater.* **28**, 2777–2781 (2016).
31. Chatterjee, T. & Wong, K.-T. Perspective on host materials for thermally activated delayed fluorescence organic light emitting diodes. *Adv. Opt. Mater.* **7**, 1800565 (2019).
32. Ochi, J. et al. Highly efficient multi-resonance thermally activated delayed fluorescence material toward a BT.2020 deep-blue emitter. *Nat. Commun.* **15**, 2361 (2024).
33. Huang, F. et al. Combining Carbazole building blocks and nu-DABNA Heteroatom alignment for a double boron-embedded MR-TADF emitter with improved performance. *Angew. Chem. Int. Ed.* **62**, e202306413 (2023).
34. Yadav, R. A. K., Dubey, D. K., Chen, S. Z., Liang, T. W. & Jou, J. H. Role of molecular orbital energy levels in OLED performance. *Sci. Rep.* **10**, 9915 (2020).
35. Zhang, K. et al. Carbazole-decorated organoboron emitters with low-lying HOMO levels for solution-processed narrowband blue hyperfluorescence OLED devices. *Angew. Chem. Int. Ed.* **62**, e202313084 (2023).
36. Oda, S. et al. Carbazole-based DABNA analogues as highly efficient thermally activated delayed fluorescence materials for narrowband organic light-emitting diodes. *Angew. Chem. Int. Ed.* **60**, 2882–2886 (2021).
37. Smith, M.B., March, J. March's Advanced Organic Chemistry: Reactions, Mechanisms, and Structure, Edn. Sixth (2006).
38. Liu, R., Gan, Z., Shinar, R. & Shinar, J. Transient electroluminescence spikes in small molecular organic light-emitting diodes. *Phys. Rev. B* **83**, 245302 (2011).
39. Weichsel, C. et al. Storage of charge carriers on emitter molecules in organic light-emitting diodes. *Phys. Rev. B* **86**, 075204 (2012).
40. Chan, C.-Y. et al. Stable pure-blue hyperfluorescence organic light-emitting diodes with high-efficiency and narrow emission. *Nat. Photon.* **15**, 203–207 (2021).
41. Oda, S. et al. One-shot synthesis of expanded heterohelicene exhibiting narrowband thermally activated delayed fluorescence. *J. Am. Chem. Soc.* **144**, 106–112 (2022).

42. Uemura, S. et al. Sequential multiple borylation toward an ultrapure green thermally activated delayed fluorescence material. *J. Am. Chem. Soc.* **145**, 1505–1511 (2023).
43. Frisch, M.J. et al. Gaussian 16, Revision A.03. (Gaussian, Inc., Wallingford CT, 2016).
44. Reimers, J. R. A practical method for the use of curvilinear coordinates in calculations of normal-mode-projected displacements and Duschinsky rotation matrices for large molecules. *J. Chem. Phys.* **115**, 9103–9109 (2001).
45. Humphrey, W., Dalke, A. & Schulten, K. V. M. D. Visual molecular dynamics. *J. Mol. Graph.* **14**, 33–38 (1996).
46. Lu, T. & Chen, F. Multiwfn: A multifunctional wavefunction analyzer. *J. Comput. Chem.* **33**, 580–592 (2012).

## Acknowledgements

This work was supported by the National Natural Science Foundation of China (Grant Nos. 52130304 (X.-H.Z.), 52422309 (K.W.), 52373193 (K.W.), 52403240 (X.-C.F.)), the National Key Research & Development Programme of China (Grant nos. 2020YFA0714601 (K.W.) and 2020YFA0714604 (K.W.)), the Science and Technology Project of Suzhou (No. ZXL2022490 (K.W.)), the Natural Science Foundation of Jiangsu (BK20230507 (X.-C.F.)), the Jiangsu Funding Programme for Excellent Postdoctoral Talent (2023ZB515 (X.-C.F.)), the China Postdoctoral Science Foundation (2023M742523 (X.-C.F.)), the China National Postdoctoral Programme for Innovative Talents (BX20230254 (X.-C.F.)), the Suzhou Key Laboratory of Functional Nano & Soft Materials, the Collaborative Innovation Centre of Suzhou Nano Science & Technology, the 111 Project (X.-H.Z.). X.T., T.H., and C.A. acknowledge Japan Science and Technology Agency (JST) CREST (Grant no. JPMJCR22B3), the Japan Society for the Promotion of Science (JSPS) Specially Promoted Research (Grant no. 23H05406), and JSPS International Leading Research (ILR) (Grant no. 23K20039). X.T. acknowledges support from JSPS KAKENHI (Grant no. 22K20536).

## Author contributions

X.T. conceived the idea and designed the project. X.T., K.W., C.A., and X.-H.Z. supervised the project. X.-C.F. and K.W. designed and synthesized the compounds. X.-C.F. carried out the theoretical simulations with the help of X.-K.C. X.-C.F. and T.-Y.Z. fabricated the OLED devices under the supervision of X.T. X.-C.F. performed the photophysical measurements with the help of S.K. and T.-Y.Z. X.T. conducted the transient EL measurements. X.T. and X.-C.F. analysed the data and wrote the manuscript. J.Y., X.-K.C, and T.H. commented on the paper. All the authors discussed the results and commented on the final manuscript.

## Competing interests

The authors declare no competing interests.

## Additional information

**Supplementary information** The online version contains supplementary material available at https://doi.org/10.1038/s41467-025-60172-y.

**Correspondence** and requests for materials should be addressed to Xun Tang, Kai Wang, Chihaya Adachi or Xiao-Hong Zhang.

**Peer review information** *Nature Communications* thanks Min Hyung Lee, Chih-Hsin Chen and Suman Kuila for their contribution to the peer review of this work. A peer review file is available.